Modeling 3D unsteady sheet cavities using a coupled UnRANS-BEM code

by
Georges L. Chahine and Chao-Tsung Hsiao
DYNAFLOW, INC.
7210 Pindell School Road
Fulton, MD 20759
e-mail: info@dynaflow-inc.com
http://www.dynaflow-inc.com

ABSTRACT

The flow field of a propeller blade subjected to sheet and cloud cavitation includes several complex and strongly interacting features: flow separation, turbulence, presence of vortical structures, deforming and moving free surfaces, free surface instability, and cavity break-up. To best describe this flow field we are developing a numerical scheme combining a viscous Navier Stokes code (UnRANS) and a potential code (BEM) combining the capabilities of each model to address portions of the problem and to achieve a description level that is not possible with each of the methods alone. The UnRANS code is used to describe the turbulent viscous flow around the blade, while the BEM code is used to describe the non-linear cavity free surface deformations.

In this paper we apply the developed method to study sheet cavitation dynamics on a straight and a twisted elliptical hydrofoil. We show the results obtained and discuss issues and future development efforts. Cases presented consider the influence of the cavitation number, the incidence angle, the oscillation of the foil, and the Reynolds number on the results. Also the influence on the cavity dynamics of a perturbation in the inflow field, such as in a wake is considered.

INTRODUCTION

The periodic shedding from a sheet cavity of a bubble cloud and its subsequent convection downstream followed by collapse leads to deleterious effects such as noise, erosion and vibrations which can strongly affect the expected performance of marine propellers (Bark & van Berlekom, 1978, Shen & Peterson, 1978, Brennen, 1994). Even though, this phenomenon have been observed and documented for many years, the processes by which cloud cavitation inception occurs have not been elucidated. Numerical modeling of the phenomenon remains one of the frontier problems. The flow involves several complex features --- transition zones, turbulence, presence of vortical structures; deforming and moving free surfaces; free surface instability and break-up; detachment and flow of a bubbly medium. The lack of fundamental knowledge of the basic physics at play in the problem has made simulations using conventional assumptions questionable until these assumptions have been confronted.

At this time several numerical methods have been developed. The more recent involve non-linear three-dimensional modeling of partially cavitation (Kinnas et al 1993, 1999, Pellone et al 1998, Dan and Kuiper 1999 a,b, Lange, 1996). Other approaches such as by Kubota et al. (1989) and Reboud & Delannoy (1994) consider a two-phase flow or a level set model to describe the periodic cloud shedding. Some experimental studies were also conducted to understand the mechanism of unsteady attached cavitation (Franc & Michel 1988, Tassin Leger et al 1998 a,b, Katz et al 1999). The dynamics of bubble clouds was studied among others by Brennen et al (1994), Wang and Brennen (1999), Chahine et al (1983,1992). We considered a potential flow and computed by a three-dimensional boundary element method (BEM), which efficiently and accurately describes moving boundary flows (Brebbia et al 1989, Becker 1992) the bubble dynamics. The advantages of the BEM lie in the economy of unknowns only sought on the discretized liquid domain boundaries, and in its accuracy in handling boundary deformation. Moreover the movement of the boundary is easily followed in a Lagrangian fashion using the local velocity.

In order to study sheet cavitation instability and cloud inception, we couple the BEM and the UnRANS to use the best features of each of these approaches. More particularly we modified and coupled the UnRANS code, UNCLE, developed by Mississippi State University (MSU) with DYNAFLOW's Boundary Element Method code, 3DYNAFS. UNCLE is used to accurately describe the basic physics of the viscous flow around the propeller

blade, while 3DYNAFS accurately describes the non-linear free surface dynamics of the cavities and their interaction with the viscous flow.

Overview of the method

As described in the next section our approach is justified through the use of the Helmholtz decomposition where the flow velocity is decomposed into a potential part and a vortical part. The potential part is solved using the BEM code, which is modified to account for the vortical components, both in the time stepping procedure and in the boundary conditions. The Helmholtz decomposition is carried into the momentum equation, which results in a modified Bernoulli equation involving the vortical and viscous terms. These are obtained from the Navier-Stokes computations. The two-way coupling is further accomplished with the BEM cavity model providing the free surface position and its normal speed to the Navier-Stokes solver.

Solution of the UnRANS problem provides the velocity, vorticity, and pressure fields in the whole computational domain. Using a cavitation criterion, say pressure lower than a critical pressure, regions where cavities should be present are delineated. This applies to both the region of the fluid in contact with the blade and to the bulk fluid. A fine surface discretization of these cavities / free surfaces is then automatically generated for treatment by the BEM. Initially, a Dual Reciprocity Boundary Element Method (DRBEM) (Chahine et al 1997) was used to solve a Poisson equation resulting from the Helmholtz decomposition, and which describes the potential component of the flow taking the viscous vortical effects into account. A method for direct evaluation of the df/dt terms needed on the free surfaces is however presently preferred. Using the velocities and vorticities computed by the UnRANS code, df/dt is obtained using a modified Bernoulli equation, and is used to update the values of f for the next time step. The BEM is then solved; a new cavity shape found and the cavities' grids are interpolated back to the UnRANS Eulerian grids to enable computation of the following time step. The procedure is sketched in Figure 1 and can be summarized as follows:

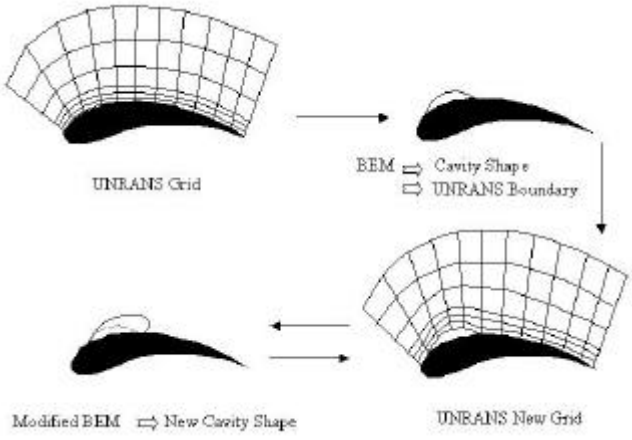

Figure 1. Sketch of the coupled UnRANS / BEM

a. The UnRANS code, using a precise discretization of the blade geometry, is used to describe the turbulent viscous flow around the blades.

b. The UnRANS equations are solved with adequate boundary conditions: no-slip velocity on solid boundaries and stress balance (i.e. zero shear and balance of normal stresses) on the cavity surfaces. This leads to knowledge of velocity, vorticity, and pressure fields in the whole computational domain.

c. In order to account for the vorticity field, a Dual Reciprocity BEM is used, which results in a Poisson equation in which the right hand side, or "source term", contains the vorticity contribution.

d. Using the velocity and vorticity field computed by the UnRANS code, the "source term" in the Poisson Equation is obtained, and is assumed invariant for the following half time step.

e. An expansion of the "source term" field in terms of a selected basis function is conducted resulting in a transformation of the Poisson equation into a Laplace equation, which is then efficiently solved using the 3DYNAFS BEM method.

f. Alternatively, to replace c-e, a Dual-BEM method is solved which directly computes df/dt using the above described source terms computed in the UnRANS procedure.

g. The BEM equations are solved using the same surface grid as the UnRANS on the blade surfaces and a fine discretization on the surface of the cavities. This results in a description of the free surface nodes velocities, which enables one to update the shape of the cavities for the next time step.

h. The cavity fine grids are interpolated back to the UnRANS grid to enable computation at the following time step, and to iterate by going back to Step a.

MATHEMATICAL FORMULATION

Let us consider a propeller blade immersed in an incompressible liquid of density r. Noting the vector velocity **u**, the time *t*, and the pressure *p*, the continuity and the momentum equations can be written:

$$\nabla \cdot \mathbf{u} = 0,$$
$$r\left[\frac{\partial \mathbf{u}}{\partial t} + (\mathbf{u}\cdot\nabla)\mathbf{u}\right] = \nabla \cdot \mathbf{t} + \mathbf{g}, \quad (1)$$

where $\mathbf{t}$ is the Newtonian stress tensor, and $\mathbf{g}$ is a body force such as the acceleration due to gravity.
In the frame of reference of the blade, the flow is subject to a no-slip condition on the rigid surface:

$$\mathbf{u} = 0. \quad (2)$$

Under some flow conditions cavitation occurs in the liquid, and cavities form over the blade surface and in the liquid. At these free surface, neglecting mass transfer across the interfaces, the liquid satisfies a kinematic and a dynamic free surface condition. The kinematic boundary condition on each surface of equation $S_i(x,t) = 0$, can be written:

$$\frac{DS_i}{Dt} = 0, \quad (3)$$

while the dynamics condition expresses the continuity of stresses at the free interfaces. If we neglect gas motion and viscous forces on the gaseous side of the free surface, only the normal components of the stresses remains, while the tangential liquid stresses are null. In this case the normal stress balance equation can be written as:

$$\mathbf{n}\cdot(\mathbf{t}\cdot\mathbf{n}) = p^i - C\,g \quad (4)$$

where p^i is the pressure on the free surface side, C the local surface curvature, and g is the surface tension. The zero stress tangential components can be written as:

$$\mathbf{t}\cdot\mathbf{n} - \left[\mathbf{n}\cdot(\mathbf{t}\cdot\mathbf{n})\right]\cdot\mathbf{n} = 0. \quad (5)$$

Cavity Model

The precise condition under which a cavity forms on a solid boundary is not yet well understood. Recently in a careful experiment Mörch and Song (1992) have shown that a perfect contact between a solid boundary and the liquid cannot exist and that nanoscopic air cavities remain at any wetted solid surface, thus forming potential cavitation nuclei. We will use this to justify the use of the following model that postulates inception of a cavity on a solid surface when the pressure at the surface drops below some critical pressure, p_c, comparable to the liquid vapor pressure, p_v, and accounting for a gas pressure, p_{go}

$$p_c = p_v + p_{go}. \quad (6)$$

If the pressure at any region is below the pressure p_c, we make that part of the surface free to move with the pressure thereafter following a polytropic gas compression law of constant, k. The space volume between the initial body surface and the freely moving free surface forms the cavity of volume V that grows and collapses on the body.
The pressure at the bubble/cavity surface is given by:

$$p = p_v + p_{go}\left(\frac{V_o}{V}\right)^k - C\,g \quad (7)$$

The cavity surface moves with the local fluid $\mathbf{u}$ subject to the condition that no cavity point can penetrate the physical solid surface of the body. During collapse a free surface point that approaches the solid surface is made a solid node again.

Mixed Approach

In order to be able to study with some accuracy the physics involved with the highly nonlinear dynamics of the cavities, especially in the boundary layer of the blade, a mixed UnRANS/BEM Eulerian / Lagrangian approach was selected. This is justified by the fact that the accurate description of the dynamics of any free surfaces in the flow domain will require a high level of discretization which *cannot* be achieved in the full computational space using an UnRANS Eulerian grid. The two codes are coupled intimately through use of half pseudo-timesteps (one for each of the methods), and through a grid "overlay" of the results of one method onto the other.

UnRANS Approach for the Liquid Behavior

In turbulent flows a wide spectrum of eddy sizes with a corresponding spectrum of fluctuation frequencies exist. The largest eddies have sizes on the same order of magnitude as the flow domain, have low frequencies, and are affected by the boundaries and the mean flow. The smallest eddies, on the other hand, are determined by the viscosity of the fluid and have high frequency fluctuations. As the Reynolds number of a given flow increases, the width of the spectrum, or the difference between the largest and smallest eddies increases.

The large eddies extract kinetic energy from the mean motion and feed it to the large scale turbulent motion. Energy is passed down the cascade to smaller and smaller eddies until viscosity causes the dissipation of the eddies. The rate of energy dissipated is determined by the large scale motion although dissipation occurs at the smallest scales. It is important to note that viscosity does not determine the amount of dissipated energy, but only the scale at which dissipation occurs, and that away from boundaries much of the physics of turbulence is effectively inviscid.

Direct numerical simulations (DNS), which involve numerically solving the full unsteady NS

equations and resolving all relevant length and time scales are currently limited to only simple flow geometries and low Reynolds numbers, as the computational resources required to resolve all length and time scales of turbulence is prohibitively expensive. Alternatively, the Unsteady Reynolds Averaged Navier-Stokes (UnRANS) equations, obtained from averaging the unsteady NS equations, require much less computational resources and have been shown to be a successful alternative (Wilson et al 1998; Gorski, 1998),

Reynolds Averaging

UnRANS equations have been shown to be successful in addressing propeller and ship flow problems, (Gorski, 1998, Wilson et al, 1998, Hsiao and Pauley 1999). They express a relationship between the mean velocity field and the mean pressure field. However, they contain as additional unknowns, the averaged products of the fluctuating velocity components, or the Reynolds stresses, $\mathbf{t}'$:

$$r\left[\frac{\partial \mathbf{u}}{\partial t}+\nabla\cdot(\mathbf{uu})\right]=-\frac{1}{r}\nabla p+u\nabla^2\mathbf{u}-\nabla\cdot\mathbf{t}'. \quad (8)$$

In order to solve these equations, additional equations relating the Reynolds stresses to the mean velocity and pressure field, are necessary (closure model). For the propeller problem, we are especially interested in a Reynolds stress closure model that exhibits, at least to the lowest order, the correct asymptotic behavior in the near-wall region, and which yields satisfactory overall predictions in that region. Otherwise, the pressures at the surface of the propeller will be poorly modeled, and the cavitation sheet will be predicted incorrectly.

We used a version of UNCLE developed at the Mississippi State University (Taylor 1991, Sheng 1995) that includes both an algebraic, Baldwin-Lomax model (Baldwin and Lomax, 1978), where the eddy viscosity is set to be proportional to the modulus of the local mean-velocity vector, and a k-e two-equations turbulence model. Here we used a simple two-layer Baldwin-Lomax model successfully used by MSU for propulsor, ship, and free surface problems. The Reynolds stresses are expressed as a function of the average velocity field, with a multiplying factor called the eddy viscosity, m_t.

$$m_t = \begin{cases} (m_t)_{inner}, & s \le s_{crossover} \\ (m_t)_{outer}, & s > s_{crossover} \end{cases} \quad (9)$$

where s is the distance normal to the solid surface. This eddy viscosities $(m_t)_{inner}$ and $(m_t)_{outer}$ are in turn written in terms of average flow characteristics involving the local vorticity and the law of the wall coordinates, y^+.

The UNCLE code is based on the artificial-compressibility method in which a time derivative of the pressure is added to the continuity equation to couple it with the momentum equations. As a consequence, a hyperbolic system of equations is formed and can be solved using a time-marching scheme. The method can be marched in pseudo-time to reach a steady state solution when a divergence-free velocity field is obtained. To obtain a time-accurate solution, a sub-iterative procedure with pseudo-time steps is performed at each physical time step.

UnRANS Free Surface Conditions

When coupling the Navier-Stokes computation with the boundary element code 3DYNAFS, the Navier-Stokes flow solver must be able to handle gas-liquid interface and moving boundaries. We have implemented in UNCLE a generalized free surface boundary conditions that enforce zero shear stress and normal stress balance on the bubble surface. For the curvilinear coordinate system with orthogonal boundaries, the boundary condition can be written as follows:

$$\begin{aligned} &\frac{\partial U}{\partial V}+g_{33}\left(g^{11}\frac{\partial W}{\partial x}+g^{12}\frac{\partial W}{\partial h}\right)=0, \\ &\frac{\partial V}{\partial V}+g_{33}\left(g^{22}\frac{\partial W}{\partial h}+g^{12}\frac{\partial W}{\partial x}\right)=0, \\ &P=p_g+p_v-Cg \\ &\quad -\frac{2}{R_e}\left(\frac{\partial W}{\partial V}+\frac{1}{2}g^{33}\left(U\frac{\partial g_{33}}{\partial x}+V\frac{\partial g_{33}}{\partial h}+W\frac{\partial g_{33}}{\partial V}\right)\right) \end{aligned} \quad (10)$$

where U,V,W are the contravariant velocities, and $x,h,$ and V are the curvilinear coordinates with W and V in the normal direction of the surface. The contravariant metrics g^{ij} and g_{ij} are defined as follows:

$$g^{ij}=\frac{\partial x_i}{\partial x_k}\frac{\partial x_j}{\partial x_k}, \quad g_{ij}=\frac{\partial x_i}{\partial x_k}\frac{\partial x_j}{\partial x_k}. \quad (11)$$

Grid Generation

To conduct the Navier-Stokes computation with moving boundaries, an efficient grid generation scheme, which can automatically generate an appropriate grid based on new boundaries at each time step, must be integrated with the Navier-Stokes solver. Here we have implemented a grid generation scheme combining both algebraic and elliptic grid generation techniques as described in (Hsiao and

Pauley, 1998) which creates a good quality grid at each time step. This uses trans-finite grid interpolation on most blocks, combined with an elliptic grid generation technique for the block including the free surface of the cavity. In this approach equations such as:

$$\nabla^2 x_i = P_i(x,h,V), \qquad i = 1,2,3, \quad (12)$$

are solved subject to given boundary conditions for the nodes on the block boundaries; i.e. known node locations at the boundary or gridlines perpendicular to the boundary. Given a problem, the strategy is to take the region on which the problem is posed, and map it onto a simple region (a cube) and calculate the metric coefficients needed to transform the differential equations and boundary conditions governing the phenomena to this simpler domain. The transformed problem is then solved using a finite difference method on the simple computational domain. Any changes to the geometry of the physical domain are performed dynamically by changing the mapping, and proceeding with the solution of the physical problem on the computational domain. We also use a multi-block method that allows only some blocks to vary discretization with times, while the other blocks remain invariant. This is very compatible with the UNCLE code, which uses multi-blocks and a multigrid approach. A typical multi-block grid for the problem here is shown in Figure 2. A time varying grid configuration (presence and absence of cavity) is shown in Figure 3.

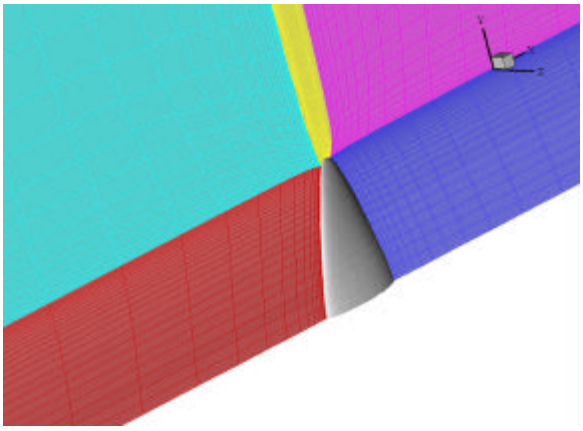

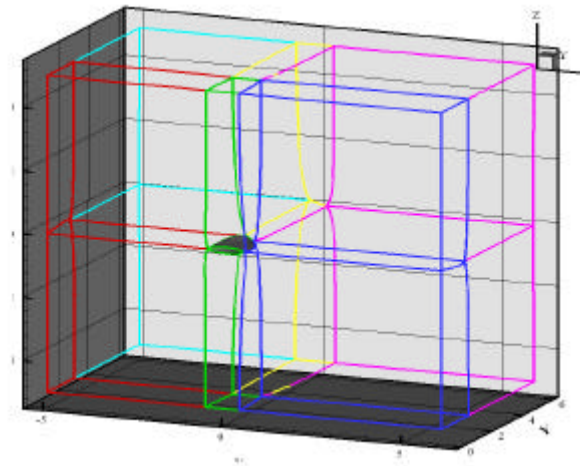

Figure 2. Multi-block gridding used in the modified UnRANS code UNCLE for the sheet cavitation problem treatment.

Treatment of the Cavity

In order to proceed with the BEM/UnRANS mixed approach we use the fact that any fluid velocity field **u** can be expressed via the Helmholtz decomposition as the sum of the gradient of a scalar potential f and the curl of a vector potential **A**:

$$\mathbf{u} = \mathbf{u}_p + \mathbf{u}_v, \quad \mathbf{u}_p = \nabla f, \quad \mathbf{u}_v = \nabla \times \mathbf{A}. \quad (13)$$

Since the flow is considered incompressible, we have

$$\nabla^2 f = 0. \quad (14)$$

By applying Green's identity one can determine f at any point **x** in the fluid domain once f and its normal derivative are known at the boundary of the domain, S, which includes submerged bodies, cavities and free surfaces:

$$W f(\mathbf{x}) = \int_S \left[f(\mathbf{x}') \mathbf{n} \cdot \nabla' G(\mathbf{x},\mathbf{x}') - \mathbf{n} \cdot \nabla f(\mathbf{x}') G(\mathbf{x},\mathbf{x}') \right] dS_{\mathbf{x}'}, \quad (15)$$

Here W is the solid angle subtended by the fluid at the point **x**, **n** is the local outward normal at the surface, and ∇' is the gradient operator in the primed variable. G is the free space Green's function,

$$G(\mathbf{x},\mathbf{x}') = -\frac{1}{|\mathbf{x}-\mathbf{x}'|}. \quad (16)$$

Taking the curl of (13) we see that **A** is directly related to the vorticity ν by

$$\nabla^2 \mathbf{A} = -\nu. \quad (17)$$

In our mixed approach the vorticity ν is obtained from the UnRANS "half step" computation.
Then, the momentum equation can be rewritten by decomposing **u** into its components:

$$\frac{\partial \mathbf{u}_p}{\partial t} + \frac{\partial \mathbf{u}_v}{\partial t} + \nu \times \mathbf{u} + \nabla\left(\frac{1}{2}|\mathbf{u}|^2\right) = -\frac{\nabla p}{r} + n\nabla^2 \mathbf{u}. \quad (18)$$

the following modified Bernoulli equation is obtained:

$$\tilde{N}\,P = -\frac{\P \mathbf{u}_v}{\P t} - \mathbf{u}\cdot v + n\tilde{N}^2\mathbf{u}, \qquad (19)$$

$$P = \frac{\P f}{\P t} + \frac{1}{2}|\mathbf{u}|^2 + \frac{p}{r}. \qquad (20)$$

This is an exact expression of the modified Bernoulli equation earlier derived in Chahine (1989, 1993).
By taking the divergence of (19) we obtain the following Poisson equation

$$\tilde{N}^2 P = R = |v|^2 - \mathbf{u}\times(\tilde{N}\cdot v). \qquad (21)$$

On the boundary, P satisfies

$$\mathbf{n}\times\tilde{N}\,P = -\mathbf{n}\times\left(\frac{\P \mathbf{u}_v}{\P t} + \mathbf{u}\cdot v - n\tilde{N}^2\mathbf{u}\right). \qquad (22)$$

The presence of the term R in the right hand side in (21) gives rise to a volume term if we were to apply the Green's identity. Therefore, (21) cannot be solved using information only at the boundary and the regular BEM. This can be overcome by applying the "dual reciprocity" boundary element method (Partridge et al 1991) as summarized below (Chahine et al. 19987). Once we obtain P, and the pressure p on the bubble surface from the dynamic boundary condition, (20) provides an expression for $\P f / \P t$ needed to update f at the following time step.

Dual Reciprocity BEM

To update the nodal values of f at the free surface at successive time steps we need to solve in an efficient way the Poisson equation for P. To do so, we expand the right hand side term R as a sum of radial functions as follows:

$$R(\mathrm{x}) = \sum_{i=1}^{N} R_i f_d(\mathrm{x}-\mathrm{x}_i) = \sum_{i=1}^{N} R_i \nabla^2 g(\mathrm{x}-\mathrm{x}_i). \qquad (23)$$

This transforms the Poisson Equation into a Laplace equation as follows:

$$\nabla^2\Psi = \nabla^2\left[\Pi - \sum_{i=1}^{N} R_i g(\mathrm{x}-\mathrm{x}_i)\right] = 0. \qquad (24)$$

Now we can use a BEM scheme similar to that for f, and obtain the field Ψ. We now have to solve the two Laplace equations, $\nabla^2 f = 0$ and $\nabla^2\Psi = 0$, with the following boundary conditions:

$$\left.\frac{\partial f}{\partial n}\right|_{solid} = -\mathbf{u}\cdot\mathbf{n};$$

$$\frac{D\Psi}{Dt} = \Pi - \frac{1}{2}|\mathbf{u}|^2 - \frac{p}{r} + \mathbf{u}\cdot\nabla f \qquad (25)$$

$$\frac{\partial\Psi}{\partial n} = \mathbf{n}\cdot\left(-\frac{\partial \mathbf{u}_w}{\partial t} + \mathbf{u}\times? + n\nabla^2\mathbf{u}\right) - \sum_{i=1}^{N} R_i \frac{\partial g_i}{\partial n}$$

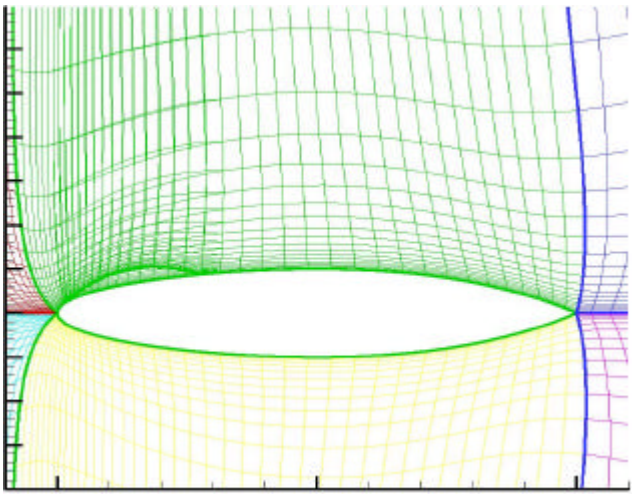

Figure 3. Grids used in the modified UNCLE code at two different steps, prior to and after sheet cavitation.

Dual BEM Approach

The computations of the function Ψ are very sensitive numerically to the choice of the radial basis functions. In addition, they require finite differencing of quantities close to the body (see Figure 5 showing the large values concentrated at the boundary and prone to large errors). These procedures, at least as we have implementing them, turned out to be not too robust. We selected to replace this scheme with a direct computation of $\P f / \P t$. If $\tilde{N}^2 f = 0$, then we also have:

$$\nabla^2\left(\partial f/\partial t\right) = 0. \qquad (26)$$

The Boundary Element Method can thus be applied to $\P f / \P t$ with the appropriate boundary conditions; i.e. zero normal derivative of $\P f / \P t$ on the solid boundary and in addition we account for the results obtained with the UnRANS code. On the solid boundaries we use:

$$p = p_{uncle}, \qquad (27)$$

to determine cavitation criterion, and on the cavity:

$$\frac{\partial}{\partial n}\left(\frac{\partial f}{\partial t}\right) = -\frac{\partial}{\partial n}\left(\frac{1}{2}|\mathbf{u}|^2 + \frac{p}{r}\right) + \mathbf{n}.\left[-\frac{\partial \mathbf{u}_w}{\partial t} + \mathbf{u}\times v + u\nabla^2\mathbf{u}\right]. \qquad (28)$$

The use of the pressures obtained by the UnRANS code is an important step that insures a perfect match between the potential flow and the Navier Stokes pressure distributions.

Discretization

The free surfaces are discretized into triangular elements, to generate a set of linear

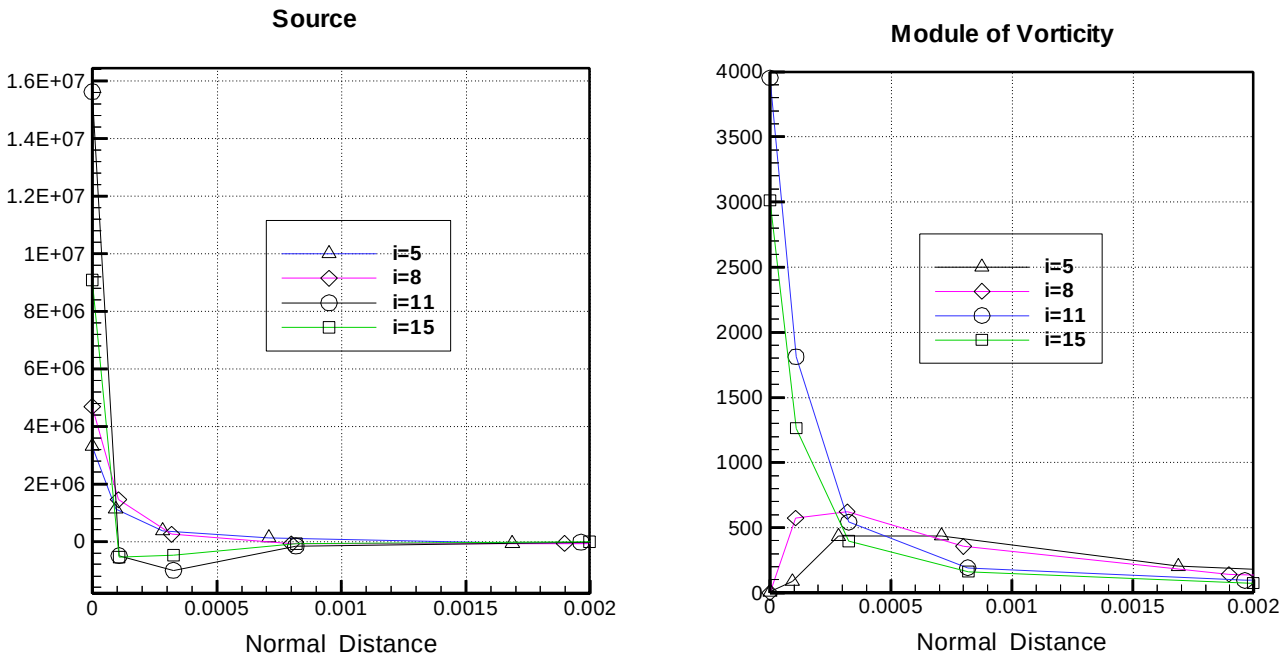

Figure 4. Concentration near the boundary of the term R in the Poisson equation. i represent the row numbers

equations relating f and $\partial f / \partial n$ (and Ψ and $\partial \Psi / \partial n$) at the nodes,

$$\sum_j \left[A_{ij}(x_i, x'_j) \frac{\partial f}{\partial n}(x'_j) - B_{ij}(x_i, x'_j) f(x'_j) \right] = 0. \quad (29)$$

The functions f and $\partial f / \partial n$ (and Ψ and $\partial \Psi / \partial n$) are linearly interpolated inside each panel using their values at the vertices of the triangle. A_{ij} and B_{ij} are geometry dependent matrices relating the influence of the j^{th} node at the i^{th} node. They are obtained by integrating the surface integral in (15) analytically over each panel separately. Since the problem has both free surface and solid boundaries, f is known on the free surface and $\partial f / \partial n$ is known on the solid boundaries. The equations are then solved for $\partial f / \partial n$ on the free surface and for f on the solid boundaries (Chahine et al, 1988, 89, 94}. (The formulation is similar for Ψ and $\partial \Psi / \partial n$).

Time Integration

The time evolution of the flow is governed by the boundary conditions. We may update the values of the velocity potential f using :

$$\frac{Df}{Dt} = \frac{\partial f}{\partial t} + \mathbf{u} \times \nabla f = P - \frac{1}{2}|\mathbf{u}|^2 - \frac{p}{r} + \mathbf{u} \times \nabla f, \quad (30)$$

where the material derivative is computed as the surface moves with the fluid. Then, the obtained normal and tangential velocities are used to determine the motion of the cavities' surface nodes. These integrations are performed with an explicit Euler scheme. An adaptive time stepping selects a time step proportional to the ratio of the smallest internodal distance to the largest nodal velocity.

Wake and Tip Vortex Modeling in the BEM

In order to properly describe the pressure and the lift distribution on the foil it is necessary with an inviscid method, to introduce additional singularity distributions to account for real fluid effects that are not directly recovered by the irrotational model. This includes, for instance a proper description of the lift of the blade, and means to describe the presence of a wake behind the foil and of a tip vortex in the blade tip area. This is a classical problem which is solved effectively by enforcing the Kutta condition at the trailing edge of the foil. This condition insures pressure equality at the trailing edge between the suction and the pressure side of the

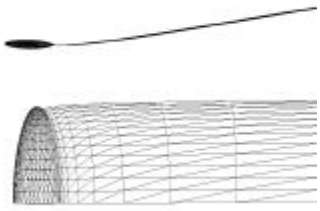

Figure 5 Foil and wake example discretization for the boundary element method.

blade. In order to achieve this we need to add a vortex sheet behind the trailing edge of the foil, which enables one through proper choice of the intensity of the vortex sheet to satisfy the following conditions:

a) Continuity of pressure across the sheet,

b) Continuity of normal velocities across the sheet,

c) Existence at each node i of a jump, Δf_i, in the velocity potential across the sheet, in order to accommodate the presence of shear or tangential velocity discontinuity.

In addition, through application of Bernoulli condition along two paths each leading to one side of the sheet, we can write that:

$$\frac{D(\Delta f_i)}{Dt} = -\frac{1}{2}\left(\left|\mathbf{u}_t^{upper}\right|^2 - \left|\mathbf{u}_t^{lower}\right|^2\right), \qquad (31)$$

where the $\mathbf{u}_t$ s are the tangential velocities on each side of the sheet.

In order to implement this concept we discretize the wake as an additional surface of the domain, (See Figure 5), and modify Green's Identity (15) to become:

$$\frac{1}{2}\left[f^{upper}(\mathbf{x}) + f^{lower}(\mathbf{x})\right] = \int_{foil}\left[f(\mathbf{x}_\sigma)\,\mathbf{n}\cdot\nabla_\sigma G(\mathbf{x},\mathbf{x}_\sigma) - \mathbf{n}\cdot\nabla_\sigma f(\mathbf{x}_\sigma)\,G(\mathbf{x},\mathbf{x}_\sigma)\right]dS_{\mathbf{x}_\sigma} + \int_{Wake}\Delta f\,\mathbf{n}\cdot\nabla_\sigma G(\mathbf{x},\mathbf{x}_\sigma)\,dS_{\mathbf{x}_\sigma}; \quad for \quad \mathbf{x}\in Foil; \qquad (32)$$

$$\frac{1}{2}\left[f^{upper}(\mathbf{x}) + f^{lower}(\mathbf{x})\right] = \int_{foil}\left[f(\mathbf{x}_\sigma)\,\mathbf{n}\cdot\nabla_\sigma G(\mathbf{x},\mathbf{x}_\sigma) - \mathbf{n}\cdot\nabla_\sigma f(\mathbf{x}_\sigma)\,G(\mathbf{x},\mathbf{x}_\sigma)\right]dS_{\mathbf{x}_\sigma} + \int_{Wake}\Delta f\,\mathbf{n}\cdot\nabla_\sigma G(\mathbf{x},\mathbf{x}_\sigma)\,dS_{\mathbf{x}_\sigma}; \quad for \quad \mathbf{x}\in Wake$$

.

A special treatment is required for the junction line between the wake and the trailing edge of the foil. Triple points are used along this line, such as illustrated in Figure 6 by nodes 1, N, and N+1. These

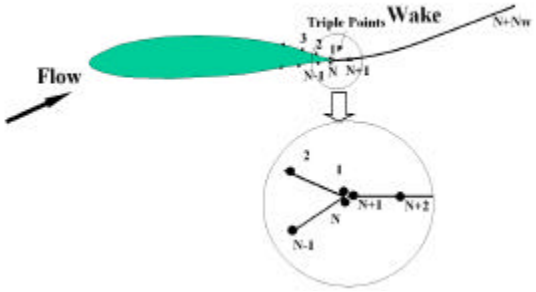

Figure 6. Illustration of the special treatment of the junction area between the wake and the foil.

are needed to enable the presence of a velocity potential jump between nodes 1 and N, and of a dipole distribution at N+1 of intensity, $\Delta f_{N+1} = f_N - f_1$. The modified BEM procedure is then to obtain at each time step: a) on the foil f knowing $\partial f/\partial n$, and b) on the wake $f^{upper} + f^{lower}$ knowing Δf.

The wake / vorticity sheet could be allowed to evolve in time, and wrap up helicoidally behind the foil tip into a tip vortex. However, this is CPU time consuming and does not address the problem at hand here. In addition, since the actual wake should be recovered quite accurately by the UnRANS code, the objective here is to have in the BEM half timestep a description of the foil surface that is not too much different from the real fluid one. Therefore, we use a fixed wake, and account for its wrapping into a tip vortex by adding a free to deform vortex line composed of a succession of linear segments, and ending with a semi-infinite vortex line as sketched in Figure 7. The velocity induced by all of these line vortices of length, dc_i, at a field point, **x**, is obtained using the Biot-Savart law:

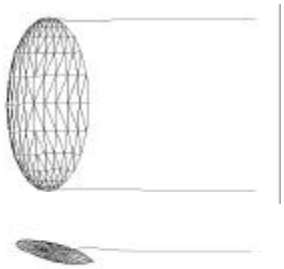

Figure 7. Sketch of the line vortices added to the blade gridding

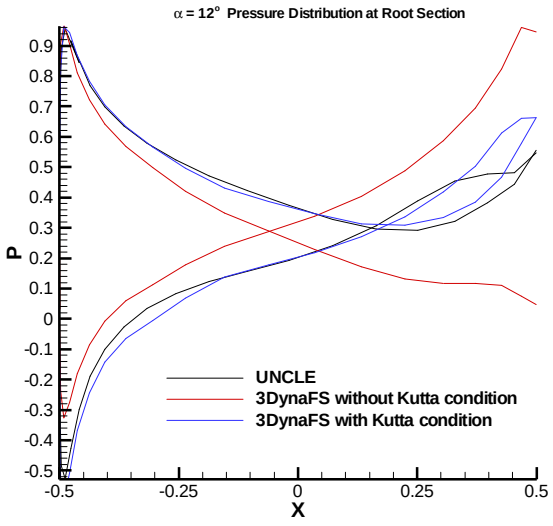

Figure 8. Pressure coefficient distribution on both sides of the blade computed with the Navier Stokes code and with the inviscid code with and without the Kutta condition applied.

$$\mathbf{u}_w(\mathbf{x},t) = \frac{1}{4p}\sum_i \Gamma_0 \frac{d?_i(\mathbf{x}-?_i)}{|\mathbf{x}-?_i|^3} k\left(\frac{|\mathbf{x}-?_i|}{\Delta}\right), \qquad (33)$$

$$\Gamma_0 = \nabla f_{TE}\big|_{Root\ Section}.$$

The potential due to the line vortices is added to the incoming flow velocity potential in order to properly compute the velocity and pressure fields.

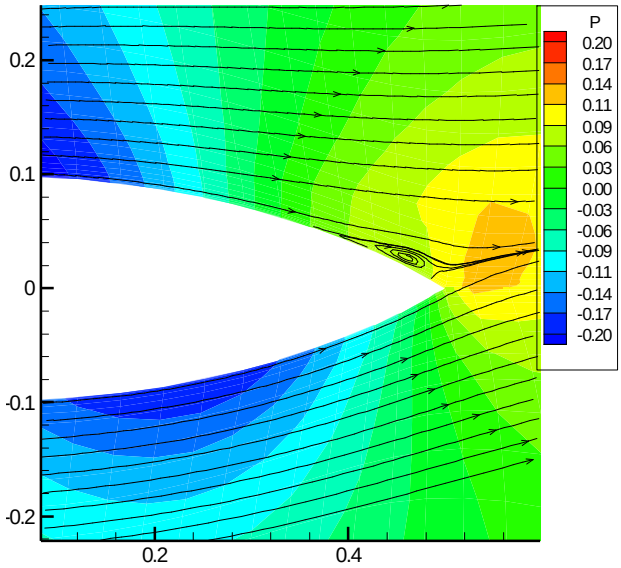

Figure 9. Pressure distribution and velocity contours near the trailing edge showing separation in the region where the cp coefficient of the BEM did not match the RANS computations in Figure 9.

With the addition of these two vorticity distributions, the BEM method is capable of recovering the pressure distribution quite accurately everywhere but in areas where separation occurs. For instance Figure 8 shows the pressure distribution at mid-span on both sides of the foil discussed below in the results section for an angle of attack of 12 degrees. The figure compares the results of the Navier Stokes code with those of the BEM code when the Kutta condition is and is not accounted for. Near the trailing edge, a separation area exists for this high incidence angle, that is captured by the RANS code (see Figure 9), but obviously not with the simple wake model BEM code. Again, the objective here of using the coupled codes is to compensate for the lack of precision in some areas of the BEM, but it is advantageous for the numerical simulations to minimize the differences between the potential and viscous code so that the vortical part is more easily computed.

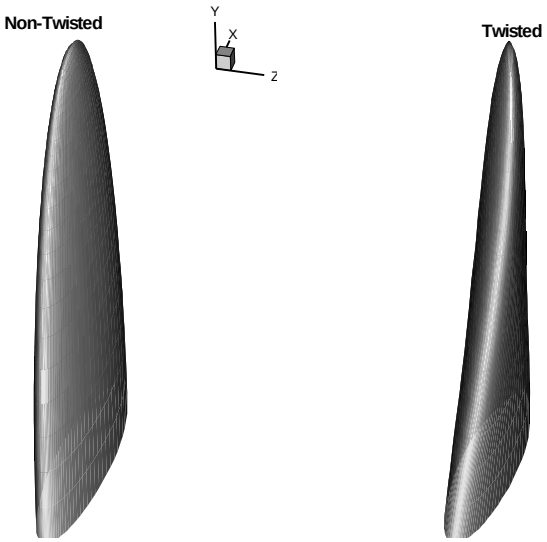

Figure 10. NACA 16-020 foil used for code development. Straight and twisted versions.

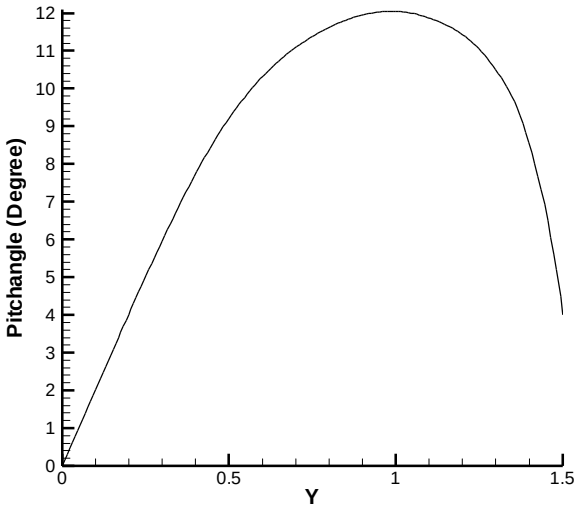

Figure 11. Pitch angle selected for the NACA foil shown in Figure 10.

RESULTS AND DISCUSSIONS

To test the developed numerical methods we selected to use a 3D elliptical hydrofoil with a NACA 16-020 cross-section, which was extensively tested experimentally in the hydrodynamic tunnel of the University of Grenoble (Boulon, 1996). A rendering of the shape of the foil is seen in Figure 10. Also shown in Figure 10 is a twisted version of this foil, with the pitch angle was varied along the span as shown in Figure 11 to minimize tip vortex cavitation. The chord of the foil is equal to 12 cm and its half-span length is 18 cm. Figure 12 is a picture taken from Boulon and Chahine (1998) and shows the development of a sheet cavity on the foil when the

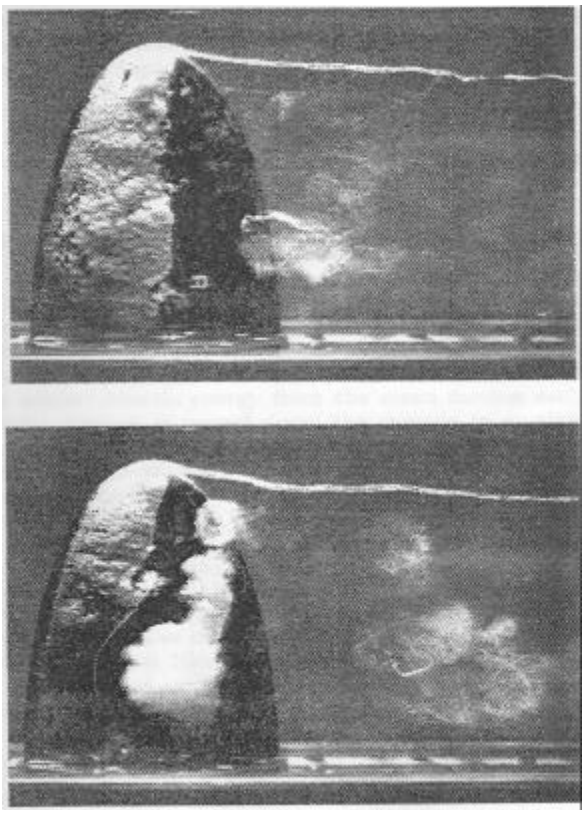

Figure 12. Sheet and cloud cavitation on an oscillating NACA 16-020 foil. Pictures taken in Grenoble. V=10 m/s, s =1.5, and the incidence angle is 11.4 ° and 12 °.

inflow velocity is 10 m/s, the cavitation number is 1.5, and the incidence angle is 11.4° and 12°. We can see under these particular flow conditions the attached sheet cavity and the shedding of a part of the cavity into a cloud convected downstream into the flow where it collapses. One disadvantage, however , of this foil shape is the noticeable presence of a tip vortex cavity that interacts with the sheet cavity. This is in fact more important in the numerical modeling that in the experiment, because the description of the tip vortex cavity requires special treatment that we have not implemented yet, because they are beyond the scope of this study. Numerical results were then obtained using the BEM code 3DYNAFS alone, the modified UnRANS code UNCLE alone and the BEM/UnRANS coupled code that is still being developed.

The mesh of the foil was chosen to be at the beginning of the calculation denser close to the leading edge, where the cavitation inception takes place, and coarser near the trailing edge. A regridding scheme was then implemented to redistribute the nodes properly once a sheet cavity develops and tends with the 3DYNAFS grid moving

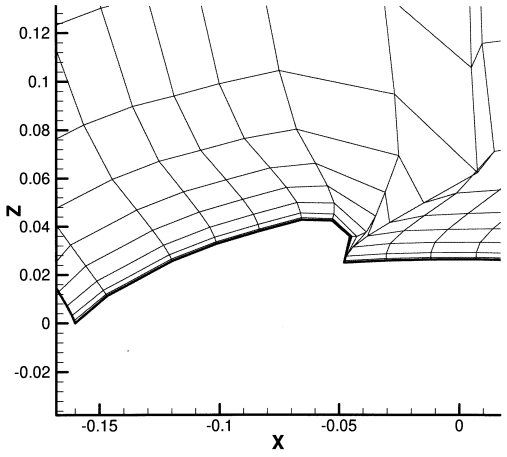

Figure 13. Crosscut of an unacceptable UnRANS grid that results when the reentrant jet starts developing

with the liquid velocity to increase the node density near the trailing edge of the cavity. This procedure and its continuous improvement and adaptation are essential for a proper operation of the developed code. In fact while regridding and adding panels and nodes, may be relatively easy for a 2D BEM, it is more challenging for the 3D code developed here, and becomes extremely difficult with the UnRANS code using regular grids as is the case for the modified version of UNCLE presently used here. In order to be able to pursue the computations shown below to a significant length of physical time, we

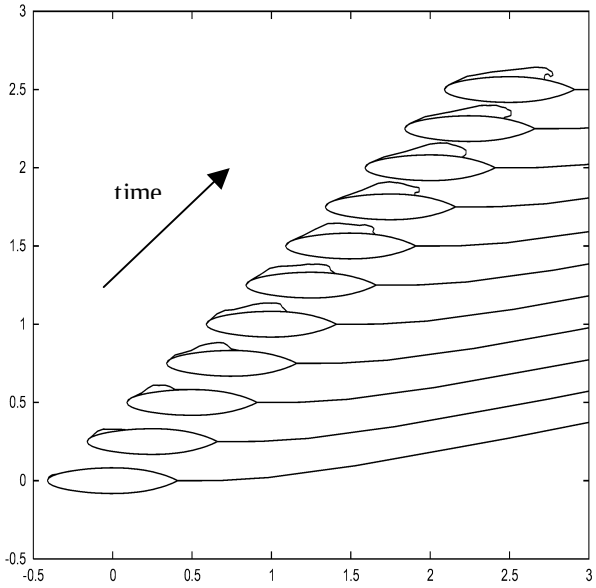

Figure 14. Time evolution of the sheet cavity and development of a reentrant jet. NACA 16-020, V=12m/s, α = 10 °, s = 0.9

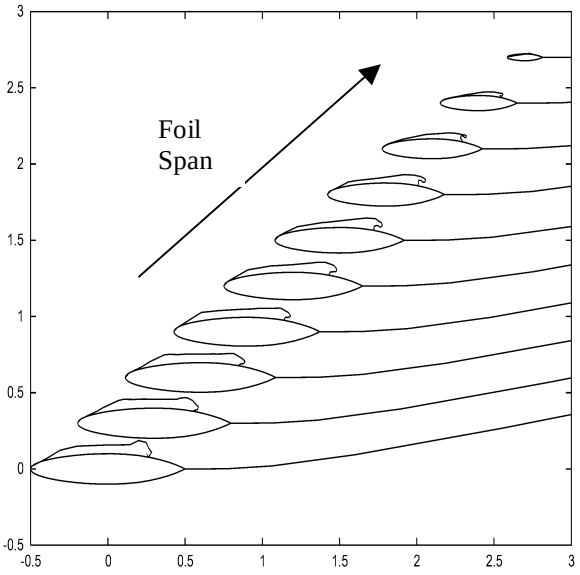

Figure 15. Snapshot at a given time of the sheet cavity along the foil span showing the 3D nature of the reentrant jet. NACA 16-020, V=12m/s, α = 10 °, s = 0.9

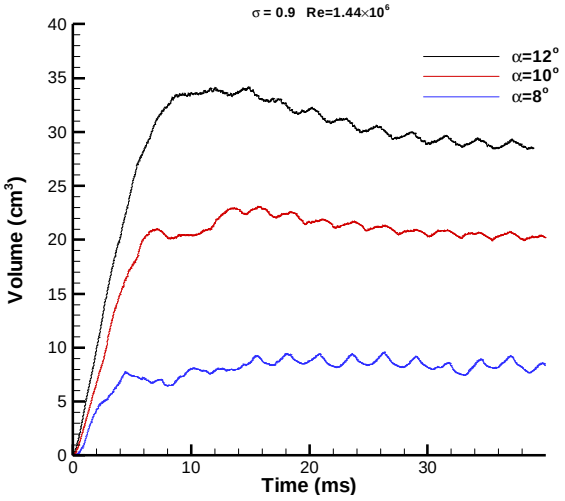

Figure 16. Sheet cavity volume versus time at different incidence angles obtained with the modified UnRANS code

had to compromise in this respect by imposing a "rounding" of the cavity near its trailing edge thus preventing the beginning of the formation of the reentrant jet. Otherwise as shown in Figure 13, the gridding scheme fails afterwards and the Navier Stokes code cannot continue the computations. Figure 13 illustrates the distortion of the grids as the reentrant jet begins to initiate. Increasing grid density at the expense of significant computation time could improve a little the picture, but a different gridding scheme, such as an overset grid scheme in the reentrant jet region is definitely needed to pursue the computations with the UnRANS beyond this point.

Figures 14 and 15 illustrate, using the BEM code 3DYNAFS alone, for an incoming flow velocity of 12m/s, and an angle of incidence α of 12°, and a cavitation number s of 0.9 the time evolution of the cavity along the foil surface. Figure 15 is a crosscut of the foil and cavity surface at 55% of the span of the NACA foil. The line behind the foil is the crosscut of the imposed vortex sheet wake. Starting from the fully wetted foil shape, the sheet cavity is seen to develop over time, form a long wavy surface, then a reentrant jet which advances under the cavity along the foil surface. At this time the code does not pursue computations after the reentrant jet hits another part of the cavity and the computation domain becomes multi-connected. However, we will be able to pursue such computation in the future, such as we have done for reentrant jet in collapsing bubbles (Zhang et al, 199*, Chahine et al, 1996). Figure 15 shows for the same flow and foil conditions a snapshot at a given time of the sheet cavity shape at various sections along the span of the foil. This figure illustrates the 3D nature of the reentrant jet which has here a funnel filament shape that touches back the top of the sheet at one end close to the tip while it is still advancing under the sheet cavity at other locations.

The volume of the cavity versus time can be seen in Figure 17. This figure also shows the influence of the angle of attack of the foil on the cavity volume variations with time. As expected the volume increases with the incidence angle, with the transient portion of the computation being also longer for the higher incidence. One can also observe some periodic volume oscillations whose relative value is larger for smaller incidence angle. This is more obvious when observing animations of the 3D results which show larger amplitude wave motion for the smaller angle of attack. Including the viscous effects in the computations result in a significant reduction of the computed sheet cavity. This is illustrated in Figure 17, which shows cavity volume versus time using both approaches for an incidence angle of 12º, an incoming speed of 12 m/s and a cavitation number of 0.9. The volumes are about 50% smaller when viscous effects are taken into account. Similarly, volume fluctuations are damped out, and as seen in Figure 17, the surface of the cavity is much smoother when viscous effects are included.

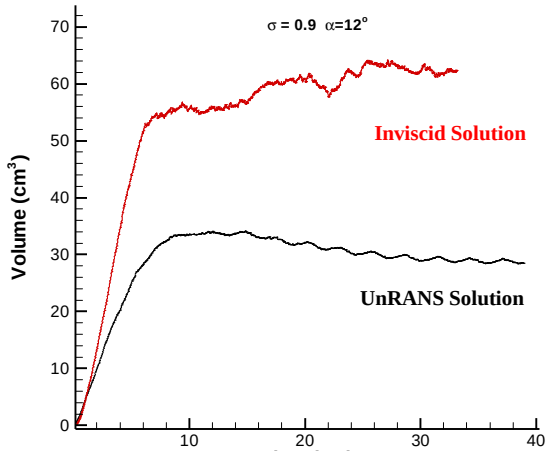

Figure 17. Comparison of the volume versus time results of the potential flow solver alone and the viscous code results.

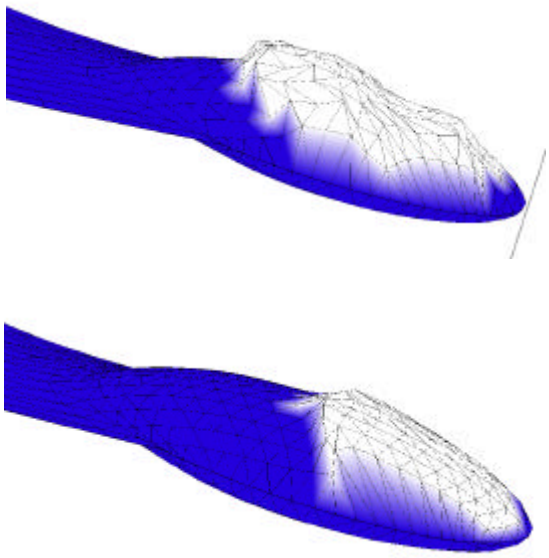

Figure 18. Shape of the sheet cavity at a given time obtained with the inviscid code alone (top) and with the UnRANS code (bottom). The back blue surface is the wake. Full volume history is in Figure 18.

This smoothing effect of viscosity is stronger for lower Reynolds numbers. Figure 19 shows for the same foil and for s = 0.9 the volume time dependence for three values of the Reynolds number, 10^5, 10^6, and 10^7. We can see from the figure that the Reynolds number has some effect on the absolute value of the cavity volume, with the tendency being as seen in Figure 17, i.e. increase volume with increased Reynolds number. In addition the volume fluctuations are seen to also increase with the Reynolds number. The same is true concerning the cavity free surface shape which become rougher with the increase of the Reynolds number. Let's restate here that stronger oscillations than those shown in the above results actually exist, since we have prevented here the development of the reentrant jet to be able to pursue the computations over a long time period.

Figure 20 shows the influence of the cavitation number on the cavity volume. Three values of s are considered 0.9, 1.0 and 1.1. Here too as expected lowering the cavitation number results in increased cavity volume and increase volume oscillations.

Figure 21 shows how the lift coefficient distribution, c_p, along the foil is modified by the development of the sheet cavity. As expected c_p is

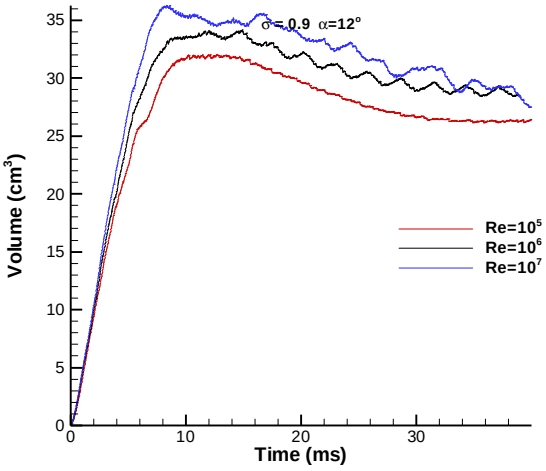

Figure 19. Influence of the Reynolds number on the sheet cavity volume time variations.

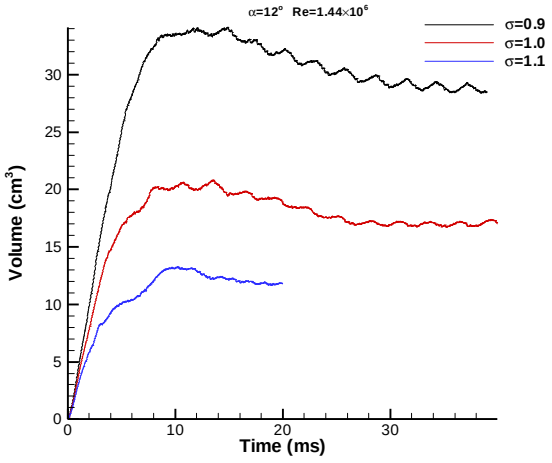

Figure 20. Influence of the cavitation number on the sheet cavity volume time variations.

very much modified on the suction side taking the value - *s* at the location of the cavity. Here, we also see that the pressure side pressures are also affected along the full length of the foil and drop by more than 10% further resulting in loss of lift.

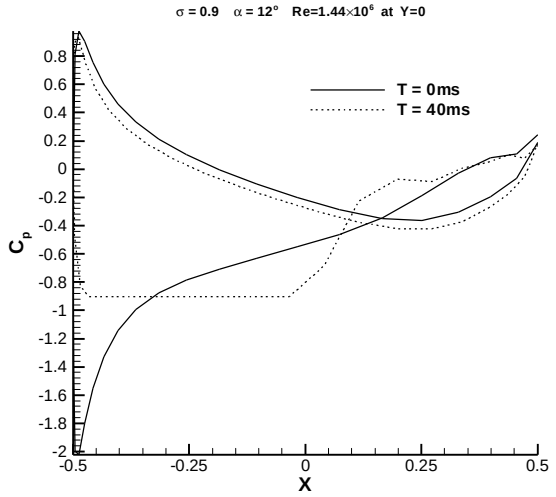

Figure 21. Modification on the lift coefficient on the NACA16-020 foil with the development of the sheet cavity.

c) Non-uniform wake-like inflow conditions.

We have already seen in Figure 10 a rendering of the shape of the twisted NACA 16-020. Figure 11 showed the values of the imposed pitch angle. Figure 22 compares the resulting pressure coefficient distribution over the blade surface between the straight and the twisted foils. With the pitch angle being reduced near the tip and the root we have aimed at generating sheet cavitation only over the mid-span of the blade. The actual shapes of the cavities generated on the twisted and untwisted foils can be seen in Figure 23. The cavitation in the twisted case for this configuration appears to be away from the root, where the incidence angle is zero. The change in the pressure distribution as the sheet cavity develops can be seen in Figure 24. Finally Figure 25 shows the difference in the cavity shape and in the flow field pressure distribution at a selected time and at various span locations over the foil.

In order to check if the code is able to handle properly incoming oscillations in the flow field we considered a uniform velocity at infinity oscillating between 6 and 12°. This resulted as expected in strong oscillations of the volume as shown in Figure 26.

Finally a wake-like non-uniform flow field

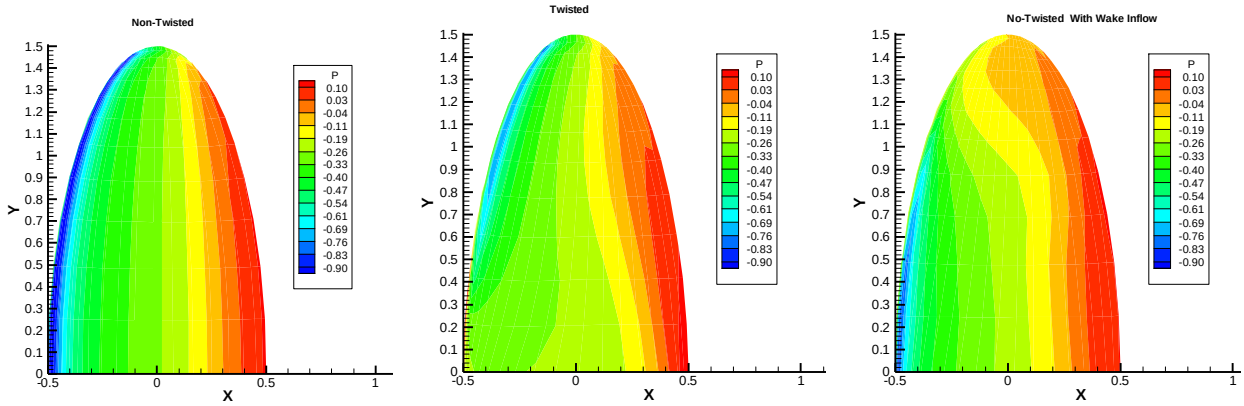

Figure 22. Comparison of the pressure distribution on the fully wetted foil under three conditions: a) Non-twisted foil in a uniform flow field, b) Twisted foil in a uniform flow field, and c) Non-Twisted foil in a wake-like flow field

Complex 3D simulations

In order to show the capabilities of the developed codes to address complex 3D geometries and flow conditions, we consider the following effects on the sheet dynamics:

a) Presence of oscillations in the incoming flow or in the foil incidence,

b) Presence of significant twist on the blade shape, and

was imposed at the entrance to the computation domain. Figure 28 describes this flow field by representing the resulting velocity contours at the start of the computations where the foil is fully wetted. We purposely selected a wake like sinusoidal distribution in the leading edge to minimize or eliminate the tip vortex cavitation. As expected, the code operated properly under these conditions and the resulting sheet cavity volume was significantly smaller (see Figures 28 and 29) than that obtained

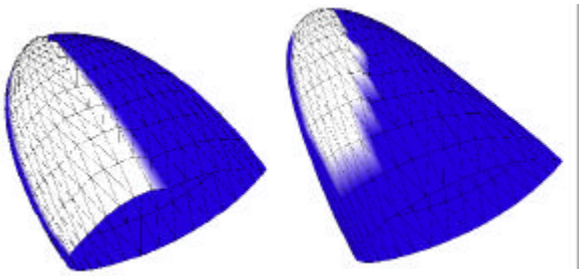

Figure 23. Shape of the cavitation region over the straight and twisted NAC16-020

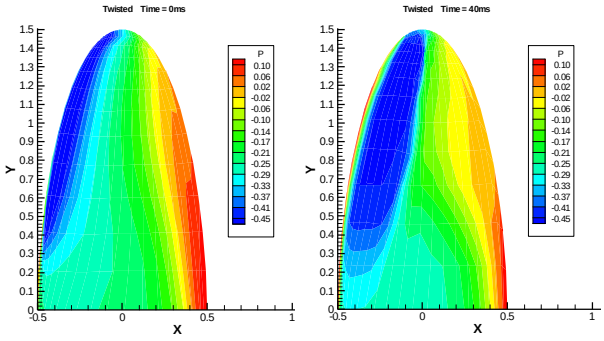

Figure 24. Change in the pressure distribution with the development of the sheet cavity.

with the uniform flow under the same condition, i.e. V=12 m/s, a =12°, and s =0.9.

CONCLUSIONS

We have developed a 3D viscous/inviscid scheme to describe sheet cavitation on propeller blades. The code uses a BEM and an UnRANS procedure to describe the cavity shape and time

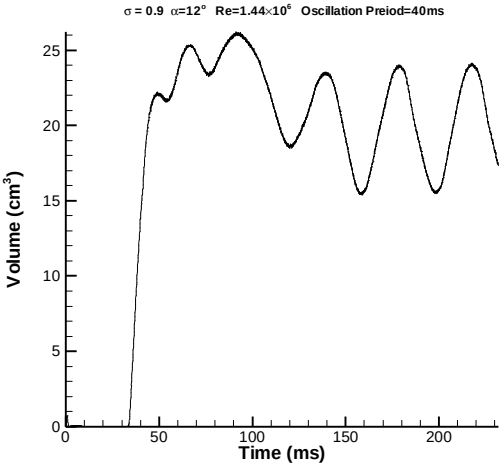

Figure 26. Time evolution of cavity volume on a NACA16-020 foil oscillating between 6 and 10 degrees with an oscillation period of 40ms.

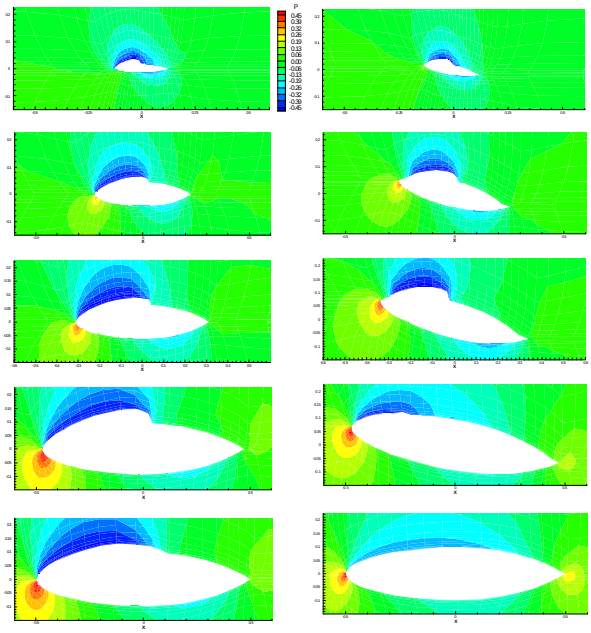

Figure 25. Cavity shape and pressure distribution in the flow field at various span locations and at a selected time. Left set is for un-twisted foil and right set is for twisted NACA16-020 foil.

evolution up to the point of formation of a reentrant jet which would result in the inception of cloud cavitation. Beyond this point further development of the codes is needed and is on-going. This development involves mainly definition of adequate grid generation procedures.

From our numerical results it appear that there are three schemes for cavity shape oscillations at various flow conditions. These may occur simultaneously under some flow conditions:

a) The oscillation of the cavity extent, i.e length, width, and height,
b) The development of a wavy over the cavity surface whose amplitude can be large enough to cut the cavity into two parts, and
c) The formation of a reentrant jet, which curls under the cavity and detaches a portion of it into a cavity cloud.

The last two conditions may lead to cloud cavitation formation.

We have also found that the Reynolds number affects the results making the cavity appearance more distorted and its volume larger at larger cavitation numbers.

ACKNOWLEDGMNETS

This work was supported by the Office of Naval Research under Contract No. N0014-97-C-0167

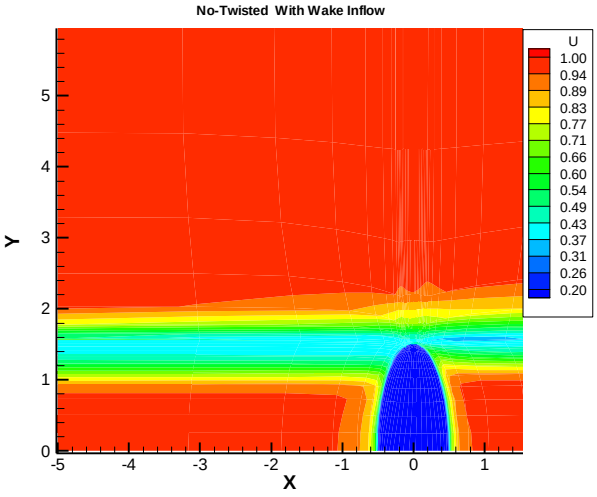

Figure 27. Non-Uniform wave-like flow field imposed around the NACA16-020 foil. Notice imposed strong velocity deficit in the tip area.

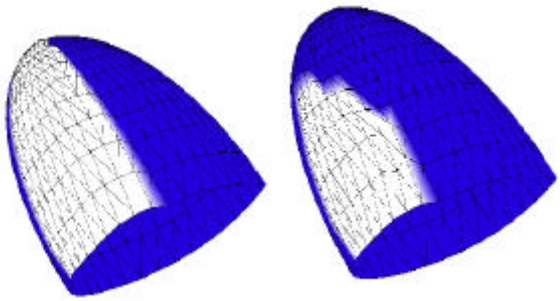

Figure 29. Cavitation distribution over the NACA16-020 foil in a uniform flow and in the wake-like non-uniform flow field described in Figure 26.

under the monitoring of Dr. Edwin Rood. This support is greatly appreciated.

REFERENCES

1. Taylor, L. K., "Unsteady Three-Dimensional Incompressible Alogrithm Based on Artificial Compressibility," Ph.D. Dissertation, Mississippi State University, Mississippi, May 1991.

2. Sheng, C., "Development of a Multiblock Multigrid Algorithm for the Three-Dimensional Incompressible Navier-Stokes Equations," Ph.D. Dissertation, Mississippi State University, Mississippi, Dec. 1994.

3. Baldwin, B. S., Lomax, H., "The Thin Layer Approximation and Algebraic Method for Separated Turbulent Flows", AIAA Paper 78-257, 1978.

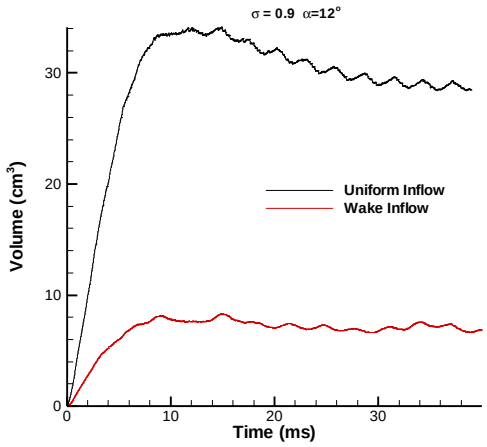

Figure 28. Comparison of the cavity volume generated on the non-twisted NACA16-020 foil in auniform field and in a non-uniform field

4. Bark, G. & van Berlekom, W. B., "Experimental Investigations of Cavitation Noise," In Proc. of the 12th Symposium on Naval Hydrodynamics, Washington, D. C., USA. National Academy Press, 1978.

5. Becker, A. A., The Boundary Element Method in Engineering, McGraw-Hill, New York, 1992.

6. Boulon, O. "Etude Experimentale de la Cavitation de Torubillon Marginal –Effects Instationnaires, de Germes et de Confinement," Thesis, Institute National Polytechnique de Grenoble, 1996.

7. Boulon, O. and Chahine, G. L., "Numerical Simulation of Unsteady Sheet Cavitation on a 3D Hydrofoil," Third International Symposium on Cavitation, Grenoble France, April, 1998.

8. Brebbia, C. and Dominguez, J., Boundary Elements an Introductory Course, McGraw-Hill Book Co., New York, 1989.

9. Brennen, C. E., "Observation of Cavitating Flows," In Proc. of the 20th Symposium on Naval Hydrodynamics, Santa Barbara, California, USA. National Academy Press, 1994

10. Chahine, G. L., "Cloud Cavitation: Theory," Proceedings, 14th Symposium on Naval Hydrodynamics, Ann Arbor, Michigan, 23-27, National Academy Press, pp. 165-195, Washington, D.C., 1983.

11. Chahine, G.L. and Perdue, T.O., "Simulation of the Three-Dimensional Behavior of an Unsteady Large Bubble Near a Structure," in A.I.P. Conference Proceedings 197: Drops and Bubbles, Third International Colloquium, ed. T.G. Wang, American Institute of Physics, New York, pp. 188-199, 1989.

12. Chahine, G. L., and Duraswami, R., "Dynamical Interactions in a Multi-Bubble Cloud," *Journal of Fluids Engineering*, Vol. 114, pp. 680-686, 1991.

13. Chahine, G. L., Duraswami, R., "Dynamical Interactions in a Multi-Bubble Cloud," *Journal of Fluids Engineering*, Vol. 114, pp. 680-686, 1992.

14. Chahine, G. L., Duraswami, R., Kalumuck, K., "Boundary Element Method for Calculating 2-D and 3-D Underwater Explosion Bubble Loading on Nearby Structures, Including Fluid Structure Interaction Effects," Naval Surface Weapons Center, Dahlgren Division, Weapons Research and Technology Department, Technical Report NSWCDD/TR-93/46, Sep. 1996

15. Chahine G. L., Sarkar, K., Duraswami, R., "Strong Bubble/Flow Interactions and Cavitation Inception," DYNAFLOW, INC. Technical Report 94003-1, 1997.

16. Dang, J., Kuiper, G., "Re-Entrant Jet Modeling of Partial Cavity Flow on Two-Dimensional Hydrofoils," *Journal of Fluids Engineering*, Vol. 121, pp. 773-780, 1999.

17. Dang, J., Kuiper, G., "Re-Entrant Jet Modeling of Partial Cavity Flow on Three-Dimensional Hydrofoils," *Journal of Fluids Engineering*, Vol. 121, pp. 781-787, 1999.

18. Franc, J. P. & Michel, J. M., "Unsteady Attached Cavitation on an Oscillating Hydrofoil," *Journal of Fluid Mechanics*, 193, 171 – 189, 1988.

19. Gorski, J. J., "Pressure Field Analysis of a Propeller with Unsteady Loading and Sheet Cavitation," Proceedings, AIAA paper ?????

20. Gorski, J. J., "The Entropy Equation Budget of Bounded Turbulent Shear Flows," *Physics of Fluids*, ?????

21. Hsiao, C.-T., Pauley, L. L. "Numerical Study of the Steady-State Tip Vortex Flow over a Finite-Span Hydrofoil," *Journal of Fluids Engineering*, Vol. 120, pp. 345-353, 1998.

22. Hsiao, C.-T., Pauley, L. L. "Numerical Computation of Tip Vortex Flow Generated by a Marine Propeller," *Journal of Fluids Engineering*, Vol. 121, pp. 638-645, 1999.

23. Kinnas, S. A. & Fine, N. E., "A Numerical Nonlinear Analysis of the Flow around Two and Three-Dimensional Partially Cavitating Hydrofoils." *Journal of Fluid Mechanics*, Vol. 254, pp. 151-181, 1993.

24. Kinnas, S. A., "The Prediction of Unsteady Sheet Cavitation," Third International Symposium on Cavitation, Grenoble, France April 1998.

25. Kubota, A., Kato, H. & Yunaguchi, H., "A New Modeling of Cavitating Flows: A Numerical Study of Unsteady Cavitation on a Hydrofoil Section," *Journal of Fluid Mechanics*, Vol. 240, pp. 59-96, 1989.

26. Lange, D.F. De, "Observation and Modeling of Cloud Formation Behind a Sheet Cavity," Thesis Univ. Twente, Enschede, April, 1996.

27. Morch, K. A., Song, J. P., "Cavitation Nuclei at Solid-Liquid Interfaces," Cavitation: Proceedings of the Institution of Mechanical Engineers, pp. 1-7, 1992.

28. Patridge, P. W. and Brebbia, C. A., and Wrobel, L. C., "The dual reciprocity boundary element method," Computational mechanics publications, Southampton, Elsevier, London, 1991.

29. Pellone, C., Maitre, T., Briancon-Marjollet, L., "Partially Cavitating Hydrofoils: Experimental and Numerical Analysis," *Journal of Ship Research*, Vol. 44 No. 1, pp. 40-58, 2000.

30. Wilson, R. , Paterson, E., and Stern, F. "Unsteady RANS CFD method for naval combatant in waves", 22nd Symposium on Naval Hydrodynamics, pp. 183-197, Washington, D.C. 1998.

31. Tassin Leger, A., Ceccio, S. L., "Examination of the Flow near the Leading Edge of Attached Cavitation. Part 1. Detachment of Two-Dimensional and Axisymmetric Cavities," *Journal of Fluid Mechanics*, Vol. 376, pp. 61-90, 1998.

32. Tassin Leger, A. Bernal, L. P., Ceccio, S. L., "Examination of the Flow near the Leading Edge of Attached Cavitation. Part 2. Incipient Breakdown of Two-Dimensional and Axisymmetric Cavities," *Journal of Fluid Mechanics*, Vol. 376, pp. 91-113, 1998.

33. Wang, Y.-C. Brennen, C. E., "Numerical Computation of Shock Waves in a Spherical Cloud of Cavitation Bubbles," *Journal of Fluids Engineering*, Vol. 121, pp. 872-880, 1999.

34. Zhang S., Duncan, J. H., Chahine, G.L. "The final stage of the collapse of a cavitation bubble near a rigid wall," *Journal of Fluid Mechanics*, 257, pp. 147-181, 1993.